Surface nano-structuring produced by spallation of metal irradiated by an ultrashort laser pulse

2014 J. Phys.: Conf. Ser. 500 112070

(http://iopscience.iop.org/1742-6596/500/11/112070)

Journal of Physics: Conference Series **500** (2014) 112070 doi:10.1088/1742-6596/500/11/112070

Surface nano-structuring produced by spallation of metal irradiated by an ultrashort laser pulse

Nail A Inogamov[1], **Vasily V Zhakhovsky**[2,3], **Sergey I Ashitkov**[3], **Yusuf N Emirov**[2], **Anatoly Y Faenov**[3,4], **Tatiana A Pikuz**[4], **Masahiko Ishino**[4], **Masaki Kando**[4], **Nobory Hasegawa**[4], **Masaharu Nishikino**[4], **Tetsuya Kawachi**[4], **Mikhail B Agranat**[3], **Alexander V Andriash**[5], **Sergey E Kuratov**[5] **and Ivan I Oleynik**[2]

E-mail: nailinogamov@gmail.com
[1] Landau Institute for Theoretical Physics, Russian Academy of Sciences, Russian Federation
[2] University of South Florida, Tampa, Florida, United States of America
[3] Joint Institute for High Temperatures of Russian Academy of Sciences, Russian Federation
[4] Quantum Beam Science Directorate, Japan Atomic Energy Agency, Japan
[5] All-Russia Research Institute of Automatics, Rosatom, Moscow, Russian Federation

Abstract. It is known that under certain conditions the complex surface nano-structures are formed after irradiation on metals by ultrashort optical and X-ray laser pulses. In the paper the mechanism of formation and final geometry of such surface structures are discussed for the case of single pulse acting on a well-polished metal surface. The typical surface structures observed in our experiments and simulations are different from well-known ripples composing a regular pattern generated by excitation of surface plasmons. By contrast with the plasmon mechanism, the observed structures have spacial scales which are order of magnitude less than the used optical laser wavelengths. We demonstrate that such structures are formed after laser irradiation due to the thermomechanical spallation of ultrathin surface layer of melt, rather than the plasmon effects, which are found to be insignificant in given conditions of a single shot and initially smooth surface. Spallation is accompanied by a strong foaming of melt followed by breaking of the foam. After several nanoseconds the foam remnants freeze up with formation of complex nano-structures on a target surface.

Response of metal to heating by ultrashort laser pulse was studied using two-temperature (2T) hydrodynamics modeling and molecular dynamics (MD) simulation. Our simulations of Al, Au, Ni and Ta showed that absorbtion of laser energy in range of $F_{abs} \sim 50 - 200$ mJ/cm^2 in a skin-layer of 10–20 nm for optical lasers or in an attenuation depth of 20–40 nm for X-ray lasers leads to high electron temperatures, which propagate supersonically into the bulk of metal. As a result, after several picoseconds of electron-ion thermal equilibration, the heated layer of molten metal $d_T \sim 100$ nm thick is formed beneath the surface. Because expansion into vacuum, the tensile wave propagates into bulk of metal and produces negative pressure. Above some critical energy deposition where the tensile stress exceeds the strength of liquid metal, many voids start to nucleate beneath the surface forming a foam-like material, which may lead to spallation (ablation) of a liquid shell, if its kinetic energy is enough to overcome the tensile strength of foam. We found that the threshold for cavitation F_{nucl} is $\sim 10\%$ less than the ablation threshold F_{abl}. Simulated evolution of a vapor-liquid foam, including breaking of large bubbles having shape of Voronoi polyhedra and freezing of liquid membranes separating neighbor bubbles with formation

of 3-D nano-structures on surface, is compared with our experimental observations carried out on optical and X-ray laser facilities. Relative importance of thermomechanical (TM) vs plasmonic (PM) ways to develop 3-D surface nano-structures by an optical pulse depends on fluence F_{abs} and number of shots N. For atomically smooth (face of crystal) initial surface and $N = 1$ the PM is absent. The PM is absent also in the X-ray case for any N since the X-ray high frequency electromagnetic waves cannot excite PM.

Figure 1 shows melting and ablation (the left side), and spallation (the right side) of free-standing gold film after irradiation. This is result of long large-scale MD simulation of Au sample with dimensions $L_x \times L_y \times L_z = 1000 \times 120 \times 16.2$ nm^3 and $114 \cdot 10^6$ atoms. Gold was simulated with embedded atom model (EAM) potential developed by a stress-matching method to reproduce material response to a wide range of applied stresses and temperatures [1,2]. Colors in figure 1 show a local atomic order parameter, where green color corresponds to solid states, while red color corresponds to molten gold. Permanent dynamic rearrangement of dislocation system near boundary between melt and crystal accompanies hydrodynamic motion. Another mobile dislocation system appears and develops around the zone of the rear-side spallation, where plastic dissipation heats the solid resulting in temperature increases by 600 K from the initial room temperature.

Figure 1. Map of local atomic order of free-standing gold film with initial thickness of 1 μm at a time of 807 ps after absorption of 100 fs optical or X-ray laser pulse arriving to the frontal left side. Absorbed energy $F_{abs} = 295$ mJ/cm^2 is twice higher than ablation threshold $F_{abl} = 137$ mJ/cm^2 for optical laser (for X-ray this threshold is smaller) and 1.5 times higher than rear-side spallation threshold of a micron sized film $F_{sp} = 193$ mJ/cm^2. The F_{sp} does not depend on laser wavelength. The spall strength of solid gold is 11.6 GPa [2]. Layer with foam had time to inflate up to 0.6 μm without any warning about future breaking of foam membranes.

Development of thick foam shown in figure 1 takes long time. It follows multiple nucleations of viable atomistic sized bubbles beginning at the time 50 ps and lasting up to the 150 ps after irradiation. Nucleation zone is wide, it covers almost all molten layer 250 nm thick. Foam exhibits ability strongly expand before the fragmentation of foam. Fragmentation is caused by decays of membranes dividing contacting bubbles. In foam with low liquid content membranes are pieces of flat planes connected into a net through three plane junctions along a curves of intersections of those three planes and through branching of the junction curves in a node. Four curves intersect in one node (topology of the net). Bubbles form domains of Voronoi polyhedra, which minimizes the total area of membranes and, thus, the surface energy.

Small hole appears in membrane when its thickness decreases down to 2-3 interatomic layers as a result of strong expansion and strong stretching of membranes, see figures 2 and 3. Initial push to formation of a hole is connected with thermal fluctuation. After appearance, the hole expands in a plane of the membrane, the particular membrane disappears, and two neighbor bubbles merge into one, larger bubble. Collapse of one membrane forming a face of polyhedron strongly disturbs the neighbor polyhedrons. Junctions, which enframe the disappeared face around the face perimeter, obtain kinks from a rim around expanding hole in membrane. From the other side, the disappearance of the face disturbs force balance in a foam. Junctions enframing the disappeared face become inside an unified membrane of a larger bubble - a descendant of the two preceding bubbles unified into one bubble. The membrane with dihedral angle tends to evolve into flat membrane. All this causes capillary oscillations visible in figure 2.

The net of membranes is stretched, since foam is dynamically connected to the spallation

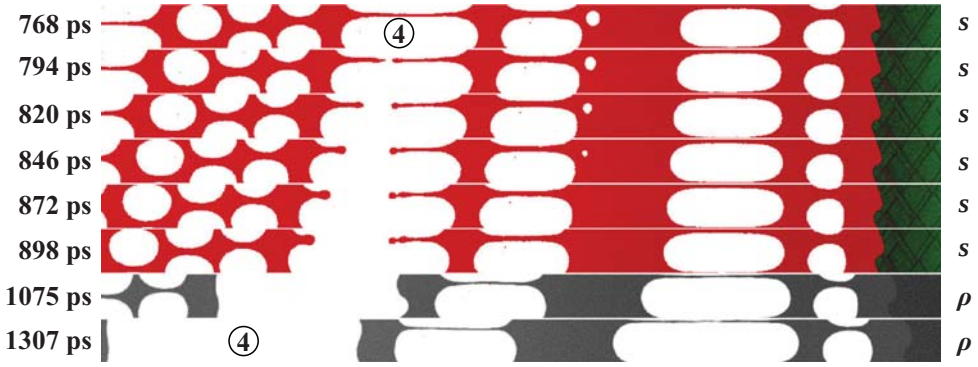

Figure 2. Rupture of membrane as a result of stretching and decrease of membrane thickness. $F_{abs} = 295$ mJ/cm^2; $x \times y$ is the plane shown. Left part of the MD box is shown only. It includes part of the foam, a layer of continuous (no voids) molten gold near the melting/recrystallization front, and solid gold with a rich family of moving and intersecting dislocations in the right part. The upper panels present maps of a local atomic order parameter s. Two bottom panels show density maps with foam after absorption of the kicks done by liquid sheets to the membranes transverse to the direction of expansion x. The sheets are the two parts of the broken membrane inside the bubble No. 4. See enumeration in figure 3b.

plate and decelerates the plate. Thickness of spallation plate, clearly seen in the head of foam in figure 1, is ≈ 40 nm. There is a vapor layer to the left of the left vapor-liquid boundary of the spallation plate. There are tensile stresses in foam; we neglect here dynamically insignificant vapor pressure. Tensile stresses appear as result of stretching. Stresses are distributed along a net of connecting membranes. Breaking of one membrane causes redistribution of stresses, decelerations, and velocities of masses in a net. Of course, this is a description of merging of bubbles and fragmentation of foam in the laterally extended foam - when many bubbles interacts in y, z directions (x is direction of expansion). In the case shown in figures 2 and 3 the MD box with $L_x \times L_y \times L_z = 925 \times 33 \times 7\,\mathrm{nm}^3$ and $12 \cdot 10^6$ atoms were used. Thus, the lateral dimensions L_y and L_z with imposed periodical conditions are not large. Two contacting bubbles in the position 4 (see enumeration in figure 3b) become a single bubble after the puncture of membrane separating them appears.

After nucleation, initially atomistic sized hole expands under action of surface tension. In figure 2 this corresponds to appearance of a gap in a membrane 4 in the time range between 768 and 794 ps. In reality the hole appears earlier than the time shown in the upper panel in figure 2, see also figures 3b,c. But finite pixel size does not allow to see the hole before its diameter d_{hole} becomes of the order of spatial period $L_z = 7$ nm of MD box in z direction. The gap in figure 2 separates two sheets - left and right - remnants of the membrane. The gap increases in size as was said under action of force directed tangentially to the surface of a sheet. Liquid, which fills the hole before the hole appearance, form a ring around the hole. Figure 3 illustrates a birth and growth of a hole. The growing hole corresponds to the deepening well in the membrane thickness profiles in figure 3c. Geometry of growing cylindrical hole is shown in figure 3a. The droplets/ring around a hole are the bumps around the well in the profiles in figure 3c. Figure 2 is a projection onto plane $x \times y$. Also it should be mentioned that there are periodic boundary conditions in y and z directions with different periods of 33 and 7 nm, respectively. Thus, that projection of the ring onto plane of figure 2 is the droplets at the end points of the sheets. It is interesting that in the case of the right sheet the edge droplet splits into pair of droplets - see the bottom red-green panel in figure 2. This pair is emphasized by the right double arrows in the bubble 4 on figure 3b.

During expansion of the hole the ring around the hole gradually accumulates mass and

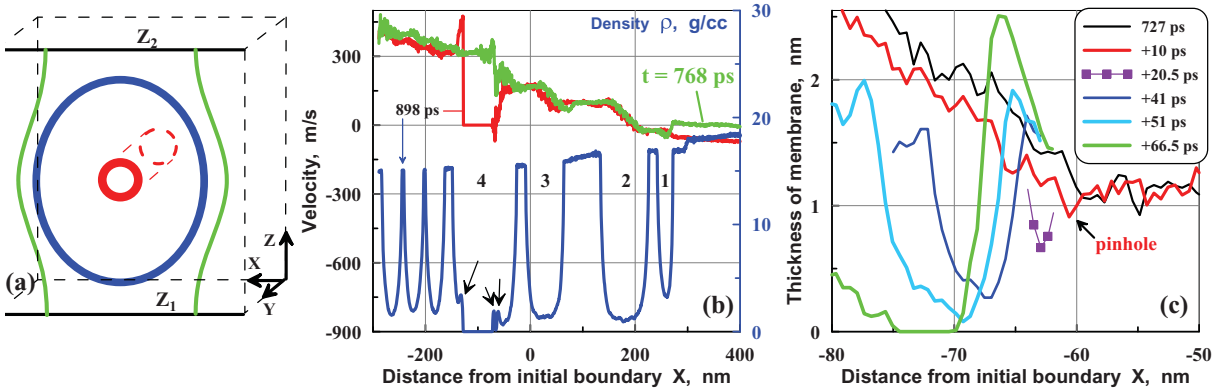

Figure 3. Decay of membrane. (a) Top view (along the axis y) of the sample presented in the plane $x \times y$ in figure 2. Here we look at the membrane going through the bubble 4 in figures 2 and 3b. It is seen how the hole in the membrane appears and develops. Colors of pinhole, expanding cylinder, and establishing strip are the same as the colors of the corresponding profiles in figure 3c. (b) Velocities $v(x, t = 768$ ps) (green) and $v(x, t = 898$ ps) (red). Those profiles correspond to the two particular times shown in figure 2. The blue curve is a density profile $\rho(x, t = 898$ ps) averaged relative to a cross-section $y \times z$. Hole in the membrane 4 is represented by the gap $v \equiv 0$, $\rho \equiv= 0$ in this profile. The moving droplets (which enframe the hole) are accelerated by surface tension to significant velocities relative to an average velocity profile. (c) Evolution of thickness of membrane $\langle h(x, t)\rangle_z$ averaged along an axis z.

momentum. These excesses of mass correspond to the density increase around the hole in figure 3b and to thickness increase in figure 3c. Evolution of the hole shown in figure 3c consists of 6 stages: (1) Before formation of cylindrical hole $t < 727 + 10ps$. (2) Emergency of pinhole with diameter $d_{hole} \sim \langle h(x, t)\rangle_z \sim 1$nm at $t \approx 727 + 10$ps. The hole is formed from viable nucleus. Geometry is explained in figure 3a. The pinhole punctures the membrane No. 4 shown in figures 2 and 3b. (3) Expansion of cylindrical hole $\langle h(x, t)\rangle_z < d_{hole} < L_z = 7$ nm, $z_2 - z_1 = L_z = 7$nm is a MD box length, see figure 3a. This expansion stage is presented by profiles $t = 727 + 20.5, +41, +51$ ps. (4) There is a transfer in the time $\approx 727 + 52$ ps from cylindrical to strip-like expansion of the hole, see figure 3a. $d_{hole} \sim L_z$ during the transfer. (5) Expansion of hole in the empty strip regime $\langle h(x, t)\rangle_z \ll d_{hole} \ll \Delta x_4$, during the time interval $779 = 727 + 52 < t < 1000$ ps, see Figure 2. Here Δx_4 is length of membrane 4, and d_{hole} is now (on the stage 5) a width of the expanding strip (not a diameter of a circular hole). The strip is an expanding gap on a profile ρ in figure 3b. (6) Collision (a kick) at a time $t \approx 1$ ns between the droplets and the transverse membranes. At this instant $d_{hole} \sim \Delta x_4$. The four first stages (1-4) are shown in figure 3c.

The impacting sheets transfer significant amount of momentum into the transverse membranes which they impact. This is clear from the velocity distribution $v(x, t)$ for the $t = 898$ ps shown in figure 3b. We see the gap $v \equiv 0$ in the distribution corresponding to the hole and we see how large are relative velocities of the droplets at the edges of the sheets. They are 163 m/s for the left droplet and 154 m/s for the right one. Relative means velocities relative to the velocities of the transverse membranes which the droplets will kick soon. Process of disappearance of membrane takes long time of ≈ 200 ps, because surface tension is rather weak As was said, the droplets are located at the edges of sheets, see figures 2 and 3. In figure 3c the droplets/ring correspond to the bumps enframing the well. In figure 3b they are the bumps enframing the gap in the density profile. The impacts of droplets into transverse membranes generates capillary oscillations. The impacts take place in the time range between the bottom red-green panel (898 ps) and the upper grey panel (1075 ps) in figure 2. For the first time we

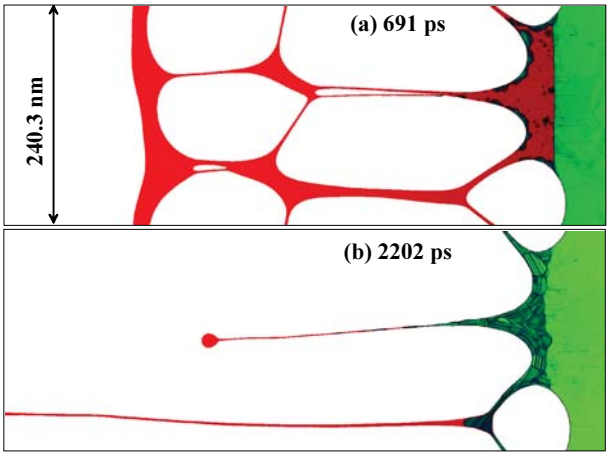

Figure 4. Expansion of foam, breaking of membranes, and freezing the remnants of membranes near the transit between foam and continuous aluminum. Absorbed energy is approximately twice large than an ablation threshold 65 mJ/cm^2. Width of sample transverse to the expansion direction x is 240 nm; $172 \cdot 10^6$ atoms. Color corresponds to atomic order parameter as on figures 1 and 2. Electron heat conductive cooling is included in this very long and large-scale MC-MD simulation.

observe excitation of capillary oscillations of the foam generated by ultrafast laser.

Frequency of those oscillations is $\omega = \sqrt{\sigma\, k^3/\rho}$, here σ is coefficient of surface tension, $k = 2\pi/\lambda$ is wavenumber, and ρ is density of liquid. Expression has been derived for the case of thick liquid layer (thick membrane) $kh > 1$, $h > \lambda/(2\pi) = 33/(2\pi) \approx 5$ nm, where h is thickness of membrane. In our case with periodic boundary conditions the wavelength λ is equal to the lateral distance 33 nm in y-direction. Density of liquid in the considered membrane is ≈ 15.5 g/cm^3. Temperature is 2250 K. We have used data from [3] to predict value of coefficient $\sigma(T = 2250\,[\mathrm{K}]) \approx 0.74 \pm 0.05$ N/m. Then $2\pi/\omega = 350$ ps. For longer waves periods will be even larger. We have followed the quarter of period of oscillation initiated by kick of the sheet into the right transversal membrane in figure 2; compare the last two panels in figure 2 – you will see that the capillary wave reverses its phase - minimum becomes maximum and vice versa. We have found that full period is ≈ 500 ps. It is larger than the calculated value 350 ps. This means that surface tension for our EAM potential for gold is lower than the value 0.74 N/m obtained above by extrapolation. Value 0.35 N/m gives period 0.5 ns. We see that surface tension of molten metal is rather weak, and the capillary periods are in the nanosecond region.

Freezing of aluminum sheets and droplets is shown in figure 4. The energy deposited in a target is $F_{abs} = 120$ mJ/cm^2, while the ablation threshold for Al is $F_{abl} = 65$ mJ/cm^2. To reproduce a complex evolution of heated surface layer a huge MD box with dimensions $L_x \times L_y \times L_z$ are $500 \times 240 \times 23.9$ nm^3, containing of 172 million of atoms, was used in MD simulation. Colors in figures 1,2, and 4 illustrate variation of local atomic order parameter, which is represented by red in liquid state and by green in solid state. This MD simulation includes Monte-Carlo description of electron heat conductive cooling which results from a large temperature gradient between surface and bulk of metal. Therefore a crystallization front, where color sharply changes from red to green, moves rather fast with velocity $v_{sol} \sim 100$ m/s from bulk molten Al (on the right side) to the membranes and sheets on the left side. It is of the

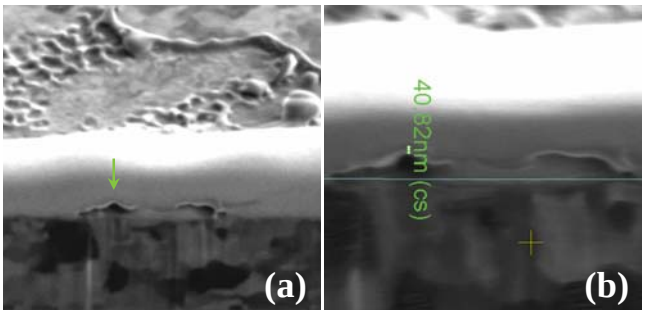

Figure 5. Focused ion beam (FIB) analysis unveils two bubbles frozen into solid Ta under surface. The left bubble is marked by the arrow in a general view (a). Thickness of the tantalum cover located above a bubble is measured in an enlarged picture (b). Height of the left bubble is 186 nm. The blue straight in (b) marks average surface.

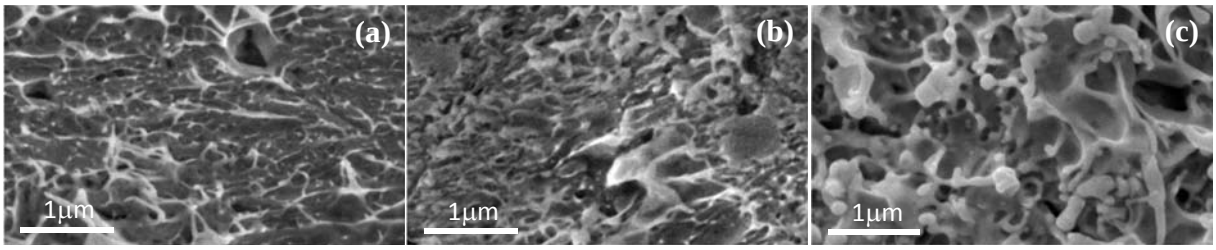

Figure 6. Enlarging of structures on gold with number of pulses N. (a) $N = 1$, (b) $N = 5$, (c) $N = 20$. High frequency soft X-ray oscillations do not excite plasmons. Outwardly structures are similar to that obtained in MD simulations, compare figures 4 and 6.

order of "velocity" of capillary oscillation $v_{cap} = \lambda_{cap}/T_{cap} \approx 140$ m/s for typical parameters $\sigma = 0.8$ N/m near melting point of Al [3] and $\lambda_{cap} = 100$ nm. Comparison of velocities v_{sol} and v_{cap} gives minimal scale of final nano-structures ~ 100 nm. Formation of structures with small sharp features is required condition with $v_{sol} \gg v_{cap}$.

Figure 5 presents studies of undersurface structures after irradiation of tantalum (Ta) by ultrafast optical laser with $\lambda = 1.2$ μm, $F_{abs} = 0.18$ J/cm^2. Two undersurface bubbles frozen into solid are clearly seen. They are similar to bubbles found in paper [4] in case of Al. But now very refractory metal is considered. We see an inclined surface of Ta above the white strip of protective layer of platinum and organic. This layer protects bubbles from ion milling.

Figure 6 shows surface structures observed on gold after irradiation by 7 ps $h\nu \approx 90$ eV laser pulses with fluence 21 ± 5 mJ/cm^2. Laser facility is described in [5]. Obtained structures shown in figure 6 are similar to the simulated one shown in figure 4 on their submicron scales and topology: there are traces of frozen sheets and junction curves with droplets. Attenuation depth 19 nm for 90 eV photons in gold is approximately the same as a skin depth for optical lasers. The only unresolved problem is rather low fluence of X-ray in comparison with F_{abs} for optical lasers which nevertheless produces similar structures.

Our simulations show that energy deposition in a thin layer of target irradiated by either X-ray or optical laser pulse leads to spallation of molten metal followed by foaming and freezing resulting in formation of complex surface nano-structures, including the frozen subsurface bubbles. Excitation of capillary oscillations of foam membranes has been detected in large-scale MD simulation of tantalum.

Acknowledgments

Authors (MBA, NAI, SIAsh) acknowledge support from RFBR grant 13-08-01095A. VVZ and IIO were supported by the NSF through grant No. DMR-1008676. AYaF and TAP were supported by RFBR grant 12-02-00947A. This work was partly supported by a Grant-in-Aid for Scientific Research (B), No. 25289244, from the MEXT, Japan. MBA, NAI, and SIAsh were supported by ROSATOM through the contract H.4x.44.90.13.1111. Simulations were performed using NSF XSEDE facilities and the USF Research Computing Cluster.

References

[1] Zhakhovskii V V, Inogamov N A, Petrov Y V, Ashitkov S I and Nishihara K 2009 *Appl. Surf. Sci.* **255** 9592–9596
[2] Demaske B, Zhakhovsky V, Inogamov N and Oleynik I 2010 *Phys. Rev.* B **82** 064113
[3] Weast R C 1980 *Handbook of Chemistry and Physics* (CRC Press, Boca Raton, FL, 61st ed.)
[4] Ashitkov S, Inogamov N, Zhakhovsky V, Emirov Y, Agranat M, Oleinik I, Anisimov S and Fortov V 2012 *JETP Lett.* **95** 176–181
[5] Ishino M et al. 2011 *J. Appl. Phys.* **109** 013504